Available online at www.sciencedirect.com
SCIENCE DIRECT
Acta Materialia 54 (2006) 483–491
Acta MATERIALIA
www.actamat-journals.com

# Stress evolution due to medium-energy ion bombardment of silicon

N. Kalyanasundaram [a], M.C. Moore [a], J.B. Freund [b], H.T. Johnson [a,*]

[a] Department of Mechanical and Industrial Engineering, University of Illinois at Urbana-Champaign, 1206 W Green Street, Urbana, IL 61801, USA
[b] Department of Theoretical and Applied Mechanics, University of Illinois at Urbana-Champaign, Urbana, IL 61801, USA

Received 2 May 2005; received in revised form 22 August 2005; accepted 21 September 2005
Available online 15 November 2005

**Abstract**

The evolution of stress in silicon, induced by argon ion bombardment up to fluences of $4.5 \times 10^{14}$ ions/cm$^2$, is studied using molecular dynamics simulations with empirical interatomic potentials. A periodically replicated 5.43 nm cube with an exposed (0 0 1) surface models the sample of silicon. An interatomic force balance method computes stresses directly across planes in the cube. After every impact, the target material is cooled to 77 K, a temperature that inhibits structural changes in the material until the next impact. This procedure makes it unnecessary to simulate explicitly any long-timescale relaxation process. For low fluences (up to about $7 \times 10^{13}$ ions/cm$^2$) the mean induced stress is tensile, but it becomes compressive with further bombardment and appears to saturate at 1.36 and 1.62 GPa when calculated from forces acting on a 5.43 nm × 5.43 nm cross-section, for the 500 and 700 eV cases, respectively. The evolution of compressive stress is observed to be directly proportional to the number of implanted argons. The results are statistically converged by ensemble averaging multiple randomized simulations.


*Keywords:* Molecular dynamics calculations; Stress evolution; Ion bombardment

## 1. Introduction

The mechanisms by which ion bombardment induces stress are not well understood, but the problem is important because of the role stress plays in numerous applications and processes. Ion bombardment leads to nanostructure formation on semiconductor [1–7], metal [8–11] and amorphous oxide [12] surfaces. Rearrangement of atoms close to the surface leads to the evolution of these ion bombardment-induced nanostructures and depends on defects created directly by the bombardment process and the instabilities associated with these defects. Strain energy gradients, or equivalently stress gradients in the material, can play an important role in the rearrangement of atoms and, therefore, in the creation of these surface nanostructures [13–18]. Thus, understanding the ion-induced stress evolution is central to understanding the nanostructure evolution on the bombarded surface. Ion processing is also widely used in very large-scale integrated (VLSI) circuits [19,20] and stress affects the semiconductor device performance significantly [21–27]. Also, the mechanical reliability of a microelectronic device depends on the stress in the material [28]. Thus, understanding and controlling stress evolution during ion bombardment could improve device performance. Argon ion bombardment at ion energies of 500 eV is also used in free-standing thin-film structures to correct out-of-plane curvature caused by large stress gradients during fabrication [29]. Curvature correction using ion beam bombardment depends on the stress induced and the mechanism of stress creation.

Stress development in thin films due to ion bombardment and ion-assisted deposition has been analyzed both numerically and experimentally. D'Heurle predicts a compressive stress due to ion bombardment using the atomic peening model [30,31]. A quantitative model studies the linear dependence of compressive stress with ion flux and the square root of the energy [32]. The dependence of stress on working gas pressures, target mass/gas mass ratio, and

* Corresponding author.
*E-mail address:* htj@uiuc.edu (H.T. Johnson).

1359-6454/$30.00 
doi:10.1016/j.actamat.2005.09.028

substrate orientation has also been studied [33]. In situ wafer curvature measurements on silicon bombarded with ion beams of MeV energy indicate an increasing compressive stress, followed by a decrease and saturation in the stress with increasing fluences [34]. Transitions between tensile and compressive stress regimes with increasing fluences have been observed in materials other than silicon [35–37]. Zhang et al. [37] have observed a steady compressive stress after a particular fluence of carbon atoms incident on a diamond lattice in the 1–75 eV ion energy range. The evolution of stresses in silicon when bombarded with medium-energy ions (~500 eV) with increasing fluences has not been analyzed in detail. The present work uses molecular dynamics (MD) simulation to study this process in silicon.

Stress in a material is dependent on the specific arrangement of atoms in the material. Any simulation technique used to study the stress evolution due to ion bombardment must, therefore, track the evolution of new atomic configurations. While various atomistic simulation techniques are available, an MD simulation allows this explicit tracking of atomic positions. Therefore, an MD simulation is used in the present work. It is also possible using MD based on empirical interatomic potentials to study fluences large enough such that stress evolution can be meaningfully interpreted. Silicon is studied due to its wide use in the semiconductor industry and the rich behavior in terms of kinetics and dynamics that the atoms near the surface exhibit when ion bombarded, which leads to the creation of nanostructures [38–40]. Beam energies used in nanostructure fabrication and curvature correction are typically less than the several keV ion beams used in ion implantation processes [19,41] and greater than the few tens of eV ion energies used in ion-assisted mild surface modification or deposition [42–48]. Two beam energies in this intermediate range, 500 and 700 eV, are considered in this work. The next section discusses the simulation methodology; a section on results and discussion follows.

## 2. Simulation methodology

In order to track the effects of the accumulated damage of multiple ion impacts, including the effects of the impacted ions themselves, it is necessary to explicitly simulate them. This is in contrast to studies of annealed damage patterns due to a single impact, which can be studied by neglecting the dynamics of the collision cascade [49,50]. Likewise, the knock-on atom method [41], which has been used to track the collision cascade dynamics in order to study defect production and structural transformation, is not able to show the effect of the embedded atoms on the stress because the method only represents the ion's energy and momentum, but not the ion itself.

In the simulations reported here, the Stillinger–Weber (SW) interatomic potential [51] models the silicon–silicon atomic interactions and the repulsive Molière potential [52,53] models the argon–silicon and argon–argon interactions. These potentials, which are widely used in molecular simulations, provide a reasonable model of the interactions of interest. Close agreement between ab initio pseudopotential-based density functional calculations and the SW potential has been demonstrated [54], and the sputtering, melting, and other phenomena due to ion bombardment calculated using the SW potential are in agreement with experiments [19,40]. The negligible attractive parts of argon–argon and argon–silicon interaction energies, when compared with the attractive part of silicon–silicon interaction energies, justify the use of a purely repulsive Molière potential for argon atom interactions [55]. The functional form of the Molière potential is

$$\Phi = Z_i Z_j \frac{q^2}{r}\left\{0.35\exp\left(-0.3\frac{r}{a}\right) + 0.55\exp\left(-1.2\frac{r}{a}\right) + 0.10\exp\left(-6.0\frac{r}{a}\right)\right\}, \quad (1)$$

where $Z_i$ and $Z_j$ are atomic numbers of the $i$th and $j$th atoms, $q$ is the electron charge, $r$ is the distance between atoms, and $a$ is the Firsov screening length dependent only on the Bohr radius and the atomic numbers [56]. The equations of motion are integrated using the velocity Verlet algorithm [57] in order to track atom trajectories. The numerical time step, $\Delta t$, is 0.25 fs except during the initial stages of ion impact when $\Delta t$ is reduced to 0.1 fs in order to resolve the initial impact dynamics. Results from simulations with even shorter time steps confirm that the chosen time steps are sufficient.

An $x$–$y$ periodically replicated 5.43 nm cube consisting of 8000 silicon atoms models the sample material as shown in Fig. 1. The transverse box size is selected so that there are no perceivable effects of the periodic boundaries; the dimension of the crystal in the $z$ direction is set so that the boundaries are far away from the impact region and the choice does not directly affect the damage characteris-

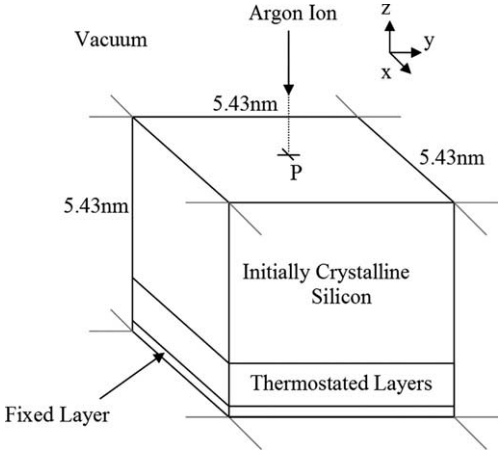


Fig. 1. Schematic of simulation cell used to perform the MD calculations of the ion bombardment process. A cell periodically replicated in the $x$–$y$ direction is used. The initially crystalline undamaged silicon cell contains 8000 atoms. The bottom few monolayers are held fixed in order to prevent translation during momentum transfer from an incident argon ion. Point $P$ represents a random impact point.

tics. Two hundred atoms at the bottom of the sample are held fixed in order to prevent translation of the target due to momentum transfer by the ions. Argon ions are incident on the sample in the $[00\bar{1}]$ direction. During an impact, a thermostat applied only to the bottom two silicon unit cells models cooling by thermal conduction into the sample. Specifically, a Berendsen thermostat [58] that works by rescaling velocities is used at each time step. The velocities are rescaled by:

$$V(t+\Delta t) = \lambda V(t), \tag{2}$$

$$\lambda = \left[1 + \frac{\Delta t}{\tau}\left(\frac{T_0}{T} - 1\right)\right]^{1/2}, \tag{3}$$

where $V(t)$ is the velocity at time $t$, $\lambda$ is the proportional scaling factor, $\Delta t$ is the time step size, $T_0$ is the target temperature, and $T$ is the current temperature of the simulation cell, and the timescale parameter $\tau$ sets the strength of the thermostat. The value of $\tau$ is $10^{-13}$ s, except during the initial stages of impact when a value of $7.5 \times 10^{-15}$ s is used. The initial $x$ and $y$ coordinates of each argon atom are selected randomly. Before every impact on the target, the same thermostat is applied to all the atoms to equilibrate the material to 77 K. Then an argon atom above the surface is assigned a momentum normal to the original silicon surface, in the process increasing the kinetic energy and the temperature of the system. After the atom impacts the surface, the thermostat in the bottom of the simulation cell is activated to cool the sample to 77 K. This thermostat temperature of 77 K is chosen because most defects in silicon are thought to be immobile for temperatures less than 150 K [59,60]. For typical fluxes used in ion bombardment, the time interval between ion impacts on a 5.43 nm × 5.43 nm surface can be a millisecond or more. However, because no structural changes should occur once the system is cooled to 77 K, there is no need to simulate the whole time gap before the next impact; this allows the simulation of fluences large enough to observe meaningful trends in stress evolution without enormous computational cost. Stresses are calculated after every impact, and the entire process is repeated for each ion impact.

There are many formulations to calculate stress at the atomistic level, none of which is universally applicable [61–63]. These formulations include the virial stress [57,64], the BDT atomic stress [65], the Hardy stress [66], the local volume method [19], the Lutsko stress [67], and the interplanar mechanical stress based on a force balance approach [68]. Theoretically, the virial stress, the Lutsko stress, the BDT stress, the Hardy stress, and the local volume method can only be usefully interpreted when the strain energy density and the stress state are homogeneous in the volume of material under consideration [61,63,69]. Cheung and Yip [68] demonstrated that the explicit mechanical and virial definitions of stress do not agree in the regions of atomic inhomogeneity like free surfaces; the methods would certainly not be expected to agree in the highly damaged inhomogeneous target material in the problem presented here. Near a surface, the virial definition has unphysical fluctuations. For the purposes of comparison, the virial stress result for the current problem is presented in Appendix A. Stress calculated using Hardy's formalism has also been demonstrated to fluctuate near the surface, though the fluctuations are considerably smaller than those in the virial formalism [69]. In using the Lutsko definition, Cormier et al. [70] point out that the presence of interfaces and system boundaries needs to be considered more rigorously because of the use of integral Fourier transforms in the calculation [69]. The interplanar mechanical traction method, described in the following paragraph, is used in the present work.

To calculate the interplanar mechanical stress, the force across a plane cutting through the material is used to compute the traction on that plane. Fig. 2 shows an example with the traction computed on a vertical $y$–$z$ plane. The traction is the equivalent force per unit area required to keep the structure in equilibrium if the structure to one side of the plane is removed. This calculation is done for a static configuration obtained by quenching, so the kinetic energy and momentum of atoms can be neglected. For the SW potential, the traction is a sum of two- and three-body forces per unit area:

$$\mathbf{t}_\mathbf{n} = \frac{1}{A}\left(\sum_i \sum_{j>i} \mathbf{F}_{ji}(\mathbf{r}_{ij}) + \sum_i \sum_{j>i} \sum_{k>j} \mathbf{F}_{jki}(\mathbf{r}_{ij}, \mathbf{r}_{kj}, \theta_{ijk})\right), \tag{4}$$

$$\mathbf{n}^i \cdot \mathbf{n}^j < 0 \qquad \mathbf{n}^i \cdot \mathbf{n}^j < 0 \text{ and/or } \mathbf{n}^i \cdot \mathbf{n}^k < 0$$

$$\sigma_{xx} = \mathbf{t}_\mathbf{n} \cdot \mathbf{e}_x, \tag{5}$$

where $A$ is the area of cross-section, $\mathbf{F}_{ji}$ is the force vector on atom $j$ from atom $i$, $\mathbf{F}_{jki}$ is the force on atom $j$ due to atoms $k$ and $i$, $\mathbf{n}^i$ is the unit vector passing through atom $i$, originating at the plane and normal to the plane, and $\mathbf{e}_x$ is the unit vector along the $x$ axis. In the present work, the traction is calculated using seven $y$–$z$ planes, each spanning the entire 5.43 nm × 5.43 nm of the simulation unit cell cross-section. The traction's depth dependence is calculated by computing the force specifically across ten smaller

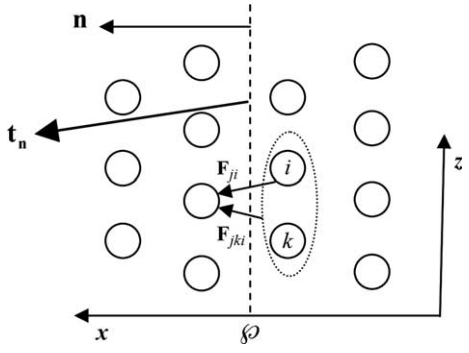


Fig. 2. Traction is calculated by determining the two- and three-body forces acting on a cross-section $\wp$ using the interplanar mechanical definition. Traction in the target box is obtained by averaging tractions calculated from seven cross-sections of size 5.43 nm × 5.43 nm. **n** denotes the normal to the plane $\wp$.

bins in each plane at different depths in the material. The $x$ coordinates of the seven planes are chosen to pass between planes of atoms in an undamaged crystal.

## 3. Results and discussion

The stress computation procedure is validated by calculating the elastic moduli of the undamaged silicon crystal using constant-strain experiments with strain magnitudes less than 0.1%. The bulk and Young's moduli are calculated to be 102.0 and 129.8 GPa, respectively, using the virial formulation, and 101.9 and 128.4 GPa using the traction method. The results in the undamaged silicon crystal at small strains are independent of the stress definition used. However, for reasons mentioned in the previous section and in Appendix A, the interplanar mechanical definition is used to calculate and interpret stress in the present work. Models based on these calculations explain the stress evolution due to ion bombardment.

Statistically converged tractions are obtained by averaging over the seven planes in each of the multiple ensembles. Fig. 3(a) and (b) show the evolution of average stresses with increasing fluences for the 500 and 700 eV beam energies, respectively. The error bars in the figures represent standard deviations of the stress values among different members of the ensemble. Averages in the 500 eV case are calculated over seven ensembles until the 100th ion and then over three ensembles beyond the 100th ion. In the 700 eV case, averages are calculated using five randomized ensembles until the 78th ion, three ensembles from the 79th to the 114th ion, and then one ensemble beyond the 115th ion.

A small initial tensile traction of 32 MPa is observed in the target prior to any impacts. This tension is a result of the imposed unit cell size of 5.43 nm, which is slightly larger than the unit cell size dictated by the SW potential. This stress is representative of the dopant-related residual stress in thin-film structures. This stress magnitude is well within

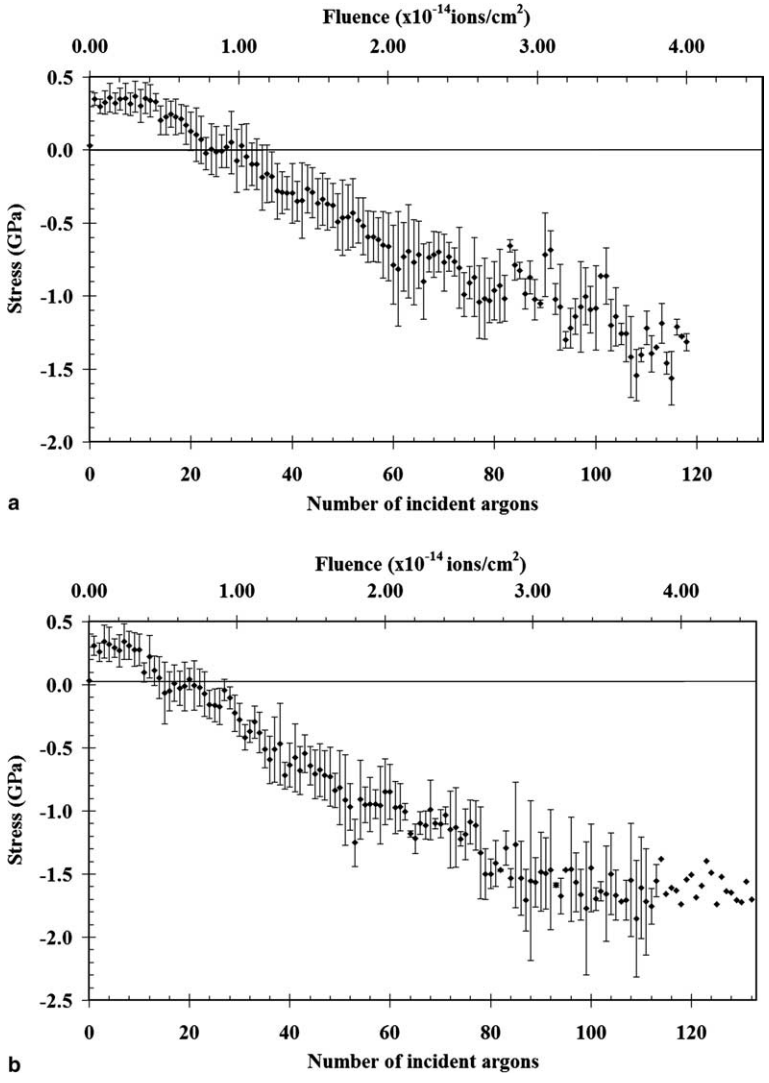


Fig. 3. Evolution of average tractions with increasing fluence for: (a) the 500 eV case and (b) the 700 eV case. Error bars indicate standard deviations from the mean in numerous statistical realizations.

the range of stresses due to thermal expansion because of temperature increases in the range of a few hundred kelvin; it is expected to have no effect on the physics of damage cascades [29].

Fig. 4 shows the variation of stress with depth into the target after an incident fluence of $2.71 \times 10^{14}$ ions/cm$^2$, together with the atomic positions from a single ensemble. It is clear, as expected, that computed stresses are higher in regions of greater damage. The nearly flat interface separating the highly damaged region and the predominantly undamaged, nearly crystalline region below becomes well defined between a fluence of $2.20 \times 10^{14}$ and $2.54 \times 10^{14}$ ions/cm$^2$ (65 and 75 ions, respectively). During this period, as the interface develops, the tractions in the damaged portion of the target are in general compressive and greater than 2 GPa when averaged over only the damaged portion of the material above the interface; the stresses drop significantly, close to zero, in the crystalline region.

The average stress variation with the number of implanted argon atoms (incident atoms minus sputtered atoms) shows three distinct stages of stress evolution (Fig. 5). The first stage is characterized by tensile traction, the second stage by a linearly increasing compression, and the final stage by an apparently steady compressive stress.

### 3.1. Stage I of stress evolution

After the first impact, the traction in the sample jumps to 300 MPa in tension and remains near this value for the next 10–15 ions (incident fluences of $3.39 \times 10^{13}$–$5.09 \times 10^{13}$ ions/cm$^2$). In this first stage of stress evolution, when portions of the initially crystalline surface are still undamaged, an atom impacting the surface creates a surface vacancy and pushes an atom in to a near-surface bulk interstitial position. The resultant instability associated with the creation of a surface vacancy causes the surface to reconstruct, which induces the initial tensile stress. This explanation can be confirmed by creating an ideal surface vacancy–bulk interstitial pair near the surface of an undamaged silicon crystal followed by relaxation at 300 K. Annealing the relaxed sample to 77 K and subsequent quenching to 4 K after creating the defect leads to a tensile stress of 64 MPa, which is consistent with the ion bombardment results. During the first few impacts, parts of the target close to the surface are still undamaged and the surface retains its tendency to reconstruct and take on tensile stress. It is only after the first 10–15 impacts that the damage affects the entire surface and renders the mechanism ineffective. A second mechanism then takes over and leads to compressive stress.

### 3.2. Stage II of stress evolution

The onset of the decrease in tensile stress marks the beginning of the nominal second stage of stress evolution. The increasing compressive stress is observed in both 500 and 700 eV ion energy cases, although the crossover from tensile to compressive occurs with fewer impacts in the 700 eV case. As shown in Fig. 5, once the entire surface is damaged, after a fluence of about $7 \times 10^{13}$ ions/cm$^2$, the compressive stress is proportional to the number of argon atoms implanted at a given depth. The rate of increase in compressive stress changes after a fluence of about $2.40 \times 10^{14}$ and $1.70 \times 10^{14}$ ions/cm$^2$ in the 500 and 700 eV cases, respectively, and marks the end of the second stage of stress evolution. Two models relating the number of implanted argon atoms to the mechanical stress are presented below. The first model is based on a supplantation mechanism, while the second is based on an implantation mechanism.

Sputtering calculations have shown that three to four silicon atoms sputter for every five incident argon atoms [71]. The first model explaining the stresses assumes that

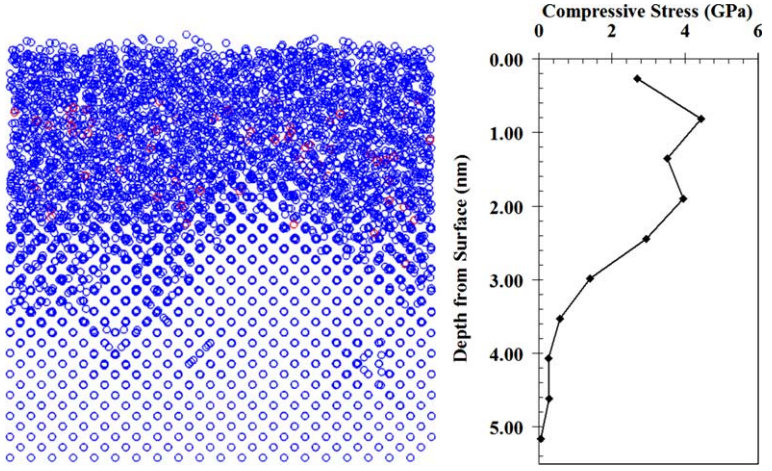


Fig. 4. Variation of stress with depth after a fluence of $2.71 \times 10^{14}$ ions/cm$^2$ in comparison to the damaged structure of the target. Atomic positions obtained from one of the ensembles are shown after the same fluence. Blue circles denote silicon atoms and red circles denote argon atoms. The structure is shown as viewed in the [0 1 0] direction. The stress values are averaged over seven cross-sections and over multiple ensembles. Consistently, higher stresses are observed in regions of greater damage.

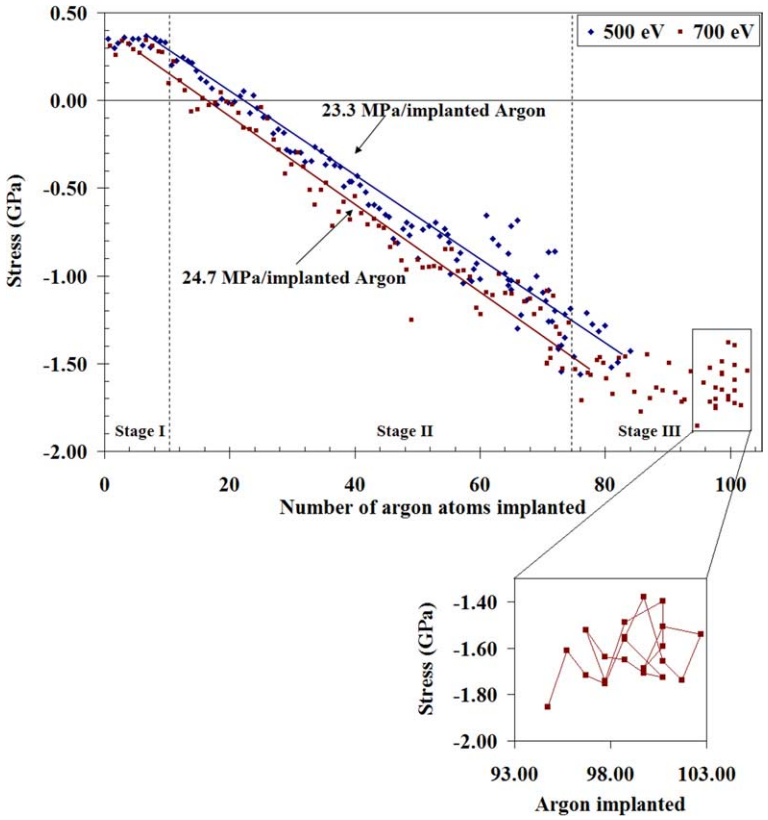


Fig. 5. Tractions plotted as a function of the number of implanted argon atoms (incident atoms minus sputtered atoms). Three stages of stress evolution are observed: an initial tension, followed by steadily increasing compression, and finally a nearly steady compression. The rate of increase in compression in the second stage is 23.3 MPa per implanted argon and 24.7 MPa per implanted argon for the 500 and 700 eV beam energies, respectively. The inset shows the variation of stress versus number of implanted argon atoms for the 700 eV case. Time (or total fluence) increases from A to B along the line joining the points. The oscillatory behavior of stress and number of implanted argons about a steady value are characteristic of the third stage of stress evolution, which represents a nearly steady state.

each incident argon atom supplants a silicon atom from the lattice and no volume changing defects are created. Since the atomic radius of an argon atom is effectively larger than a silicon atom, any argon implantation would result in increased volume. The atomic radii of silicon and argon atoms are assumed to be 0.117 nm, or half of the silicon–silicon equilibrium bond distance in crystalline silicon, and 0.188 nm, or the van der Waals atomic radius, respectively. The compressive stress required in the $x$–$y$ direction to restore the system to its original volume is calculated. Periodic boundary conditions are applied in the $x$ and $y$ directions and the sample is allowed to expand freely in the $z$ direction, replicating the boundary conditions used in MD simulation. Elastic constants $C_{11}$, $C_{12}$, and $C_{44}$ for silicon are assumed to be 143.8, 64.3, and 37.7 GPa, respectively [72]. The stress required to bring the system volume back to the original undamaged volume calculated using these elastic properties is

$$\sigma_{xx} = 22.95\left(\frac{N_{\mathrm{Ar,L}}}{N_{\mathrm{Si,L}}}\right) = 22.95\left(\frac{N_{\mathrm{Ar,V}}}{N_{\mathrm{Si,V}}}\right)^{1/2}, \tag{6}$$

where $N_{\mathrm{Ar,L}}$ and $N_{\mathrm{Si,L}}$ are the linear density of argon and silicon atoms, respectively, and $N_{\mathrm{Ar,V}}$ and $N_{\mathrm{Si,L}}$ are the number of argon and silicon atoms in a layer of target material that is 5.43 by 5.43 nm in the $x$ and $y$ directions and has a thickness $t$ in the $z$ direction. Fig. 6 shows the variation of tractions and stress calculated using the supplantation model with depth calculated for one ensemble after a fluence of $2.71 \times 10^{14}$ ions/cm$^2$. While the supplantation model provides a reasonable estimate of the stress, it fails to predict the linear dependence of stress on implanted argon. Instead, the stresses follow a square root dependence and the average stresses are over-predicted from the actual interplanar mechanical stress by about 10–40%.

In the second model, each argon atom is assumed to be implanted at a substitutional site surrounded by silicon atoms in the target. Because an argon atom does not form chemical bonds with silicon atoms, one way for an argon atom to be implanted is for the argon to be surrounded and trapped by silicon atoms in the target. The assumption that argon atoms are implanted in the substitutional site is therefore reasonable. It is noted that there are fewer argon atoms close to the surface because they can easily escape their geometric, nonbonded constraint after impact. This model does not account for the rearrangement details of the atoms due to damage. Silicon sputtering is also neglected, but is small. Since sputtering is a relaxation

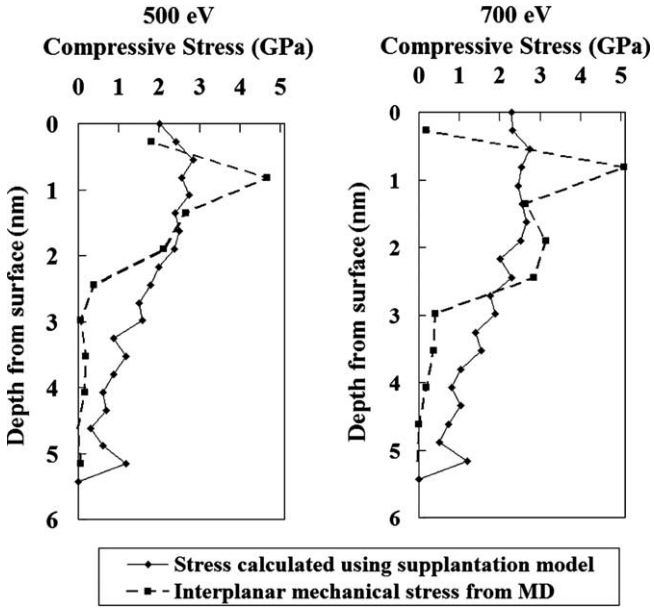


Fig. 6. Supplantation model calculations: variation of stresses calculated from MD and stresses calculated using the supplantation model. The data presented correspond to a single ensemble after a fluence of $2.71 \times 10^{14}$ ions/cm$^2$ for the 500 and 700 eV cases. The supplantation model clearly fails to predict the linear dependence of stress on the number of implanted argon atoms.

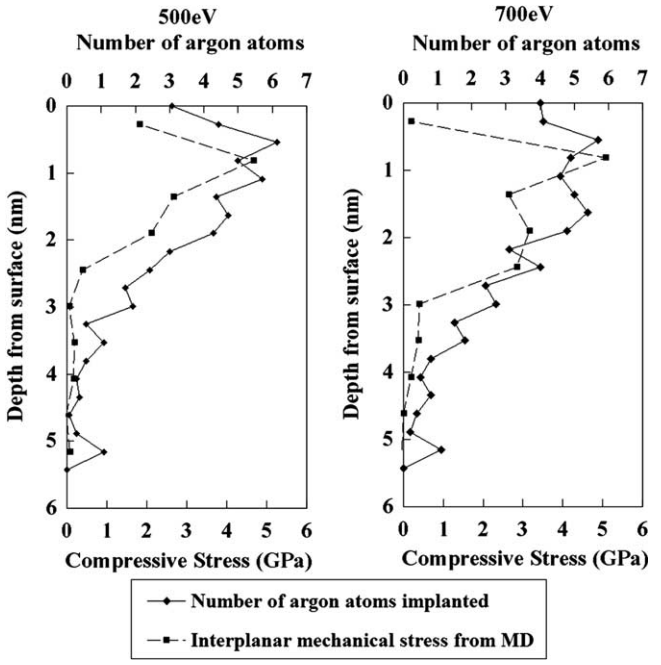


Fig. 7. Variation of stresses with depth calculated from MD and the variation of the number of implanted argons with depth from the surface for one ensemble after a fluence of $2.71 \times 10^{14}$ ions/cm$^2$. Calculations based on the implantation/substitutional model predict the direct correlation between the number of implanted argons and stresses, not just in an average sense, but also locally at any depth from the surface.

mechanism, neglecting this should result in a small overprediction of the traction. The traction is calculated analytically using the Molière and SW interatomic potentials to be 30.0 MPa per implanted argon atom, matching with the observed linear dependence upon the number of implanted argon atoms. The coefficient of linear dependence is also predicted reasonably well. MD simulation yields 23.3 MPa per implanted argon and 24.7 MPa per implanted argon for the 500 and 700 eV cases, respectively.

Fig. 7 shows the number of argon atoms at different depths from the surface plotted alongside the traction calculations from MD for a single ensemble after a fluence of $2.71 \times 10^{14}$ ions/cm$^2$. A direct correlation between the number of implanted argons and stresses exists locally at any depth in the material, not just when forces and the number of implanted atoms are calculated over the entire box.

### 3.3. Stage III of stress evolution

The number of argon atoms implanted in the target saturates at large fluences; the argon implantation to silicon sputter ratio reaches steady state at fluences beyond $2.00 \times 10^{14}$ ions/cm$^2$ [71]. A steady value of stress is indeed seen in the 700 eV case (Fig. 5) after implantation of about 80 ions (implantation rate of $2.71 \times 10^{14}$ ions/cm$^2$). This steady region constitutes a third stage of stress evolution. The inset in Fig. 5 is a parametric plot between stress and number of implanted argon atoms for increasing fluences or time. The oscillatory behavior about a mean value indicates steady state. The steady value is not as clearly seen in the 500 eV case, where fewer argon atoms are implanted up to the fluences considered in this work when compared to the 700 eV case.

The steady value of compressive traction in the 700 eV case is observed to be 1.62 GPa over a depth of 5.43 nm and the value of compression in the 500 eV case is approximately 1.36 GPa over the same depth. In experimental work on stress modification in ion-bombarded MEMS micromirrors it is estimated that there is about 1 GPa of compressive stress in the damaged region [29]. Thus, the calculations using the interatomic force balance method are in reasonable agreement with experiments.

## 4. Conclusions

Three stages of stress evolution have been identified in argon ion bombardment of an initially crystalline, clean silicon surface. Due to the disorder in the material, the virial definition of stress gives physically implausible results and the interatomic force balance-based stress definition is used to interpret the stress. In the first stage, occurring when the first few ions impact the predominantly undamaged surface, tensile stresses of about 300 MPa are observed due to creation of surface vacancies and bulk interstitials near the surface with no other significant damage to the remaining crystal. The tensile stress remains steady for the first approximately 10 impacts ($3.39 \times 10^{13}$ ions/cm$^2$). Then in the second stage of evolution, the stress decreases, becoming

compressive in direct proportion to the number of argon atoms implanted in the target. A model based on substitutional argon defects predicts this linear behavior and its coefficient. A model based simply upon the exclusional volume of the embedded argon does not. The rate of increase in compression in the second stage is 23.3 MPa/implanted argon and 24.7 MPa/implanted argon for the 500 and 700 eV cases, respectively, in good agreement with the 30.0 MPa/implanted argon atom predicted by the linear model. Stresses in the target approach a steady value in the third stage of evolution. Averaged over the entire depth of 5.43 nm of the target, these values are 1.36 and 1.62 GPa for the 500 and 700 eV cases, respectively.

## Acknowledgements

This work was supported by NSF Grant DMI 02-23821. The authors thank Prof. T.G. Bifano of Boston University for many helpful discussions.

## Appendix A. Virial stress in ion bombarded material

The virial definition of stress component $\sigma_{xx}$, in a system modeled using two- and three-body interactions, is given by

$$\sigma_{xx} = \frac{1}{\Omega}\left\{\sum_i m_i|\mathbf{v}_i|^2 + \sum_i \sum_{j>i} x_{ij} f_2^x(\mathbf{r}_i, \mathbf{r}_j) + 2\sum_i \sum_{j>i} \sum_{k>j} [x_{ij} f_3^x(\mathbf{r}_i, \mathbf{r}_j, \mathbf{r}_k) + x_{kj} f_3^x(\mathbf{r}_k, \mathbf{r}_i, \mathbf{r}_j)]\right\}, \tag{A.1}$$

where $\Omega$ refers to the system volume, $m_i$ is the mass of atom $i$, $\mathbf{v}_i$ is the velocity of particle $i$, $x_{ij}$ is the $x$ component of position vector $\mathbf{r}_{ij} = \mathbf{r}_i - \mathbf{r}_j$, $f_2^x(\mathbf{r}_i, \mathbf{r}_j)$ refers to the $x$ component of two-body force between atoms $i$ and $j$, and $f_3^x(\mathbf{r}_i, \mathbf{r}_j, \mathbf{r}_k)$ is the $x$ component of three-body interaction between atoms $i$, $j$, and $k$. The three-body terms for argon–silicon and argon–argon interactions are zero. The contribution from the term $\sum_i m_i|\mathbf{v}_i|^2$ is close to zero, in the case studied here, as the stresses are computed after quenching the material to 4 K.

When the virial definition is used to calculate stress in the damaged material studied here, increasing tension is observed with increasing fluence. Fig. 8 shows the evolution of virial stress in one randomized ensemble bombarded at 500 eV to a fluence of $2.64 \times 10^{14}$ ions/cm$^2$. For reasons mentioned in [68], the virial definition of stress cannot be meaningfully interpreted in the presence of inhomogeneities like free surfaces, or in a highly damaged target material. In the physical process considered here, increasing fluences lead to increased argon implantation in the target. Despite silicon sputtering and loss of crystallinity, the mass density of the target increases due to argon implantation. Thus, in contrast to the virial result, the implanted atoms and increased density are expected to cause compressive stress in the target because the thin film is constrained in the plane of the film. This mechanism is similar to the development of compressive stress in the atomic peening model [30,31]. Experimental observations also suggest a compressive stress in the target [29] and therefore contradict the calculations based on the virial formalism. Furthermore, argon ion bombardment at 500 and 700 eV damages only the top few nanometers of the target, so the stresses in the few nanometers closest to the surface are of primary interest [71]. The use of the interplanar mechanical definition of stress instead of virial definition eliminates the unphysical fluctuations that arise due to the presence of free surface in the region of interest [68]. For these reasons, the virial definition of stress is not used. Calculations using the interplanar definition of stress agree well with experiments both in tensile/compressive nature and in the magnitude of the stress.

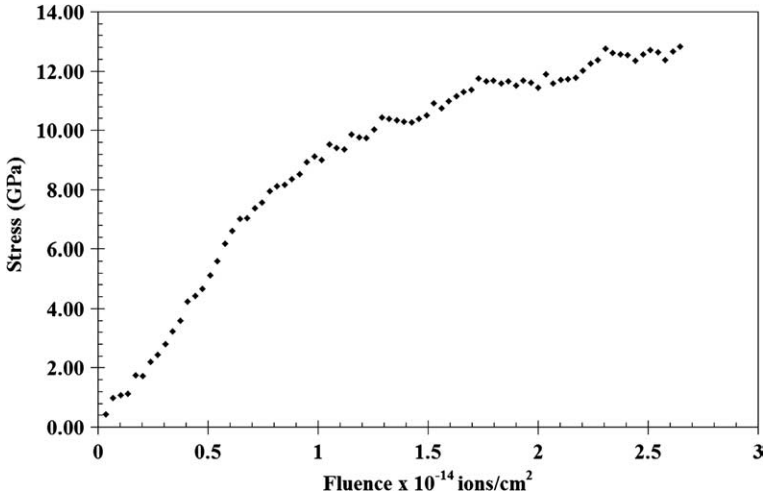


Fig. 8. Variation of virial stress with increasing fluence up to $2.64 \times 10^{14}$ ions/cm$^2$. The stress is tensile even at large fluences. This result is inconsistent with experimental observations, where compressive stresses are observed in the material at large fluences. An atomic peening model predicts a compressive stress in the material.

## References


[1] Carter G, Vishnyakov V. Phys Rev B 1996;54:17647.
[2] Fackso S, Dekorsky T, Koerdt C, Trappe C, Kurz H, Vogt A, et al. Science 1999;285:1551.
[3] Tarus J, Nordlund K, Keinonen J, Averback RS. Nucl Instrum Meth B 2000;164:482.
[4] Frost F, Schindler A, Bigl F. Phys Rev Lett 2000;85:4116.
[5] Gago R, Vazquez L, Cuerno R, Varela M, Ballesteros C, Albella JM. Nanotechnology 2002;13:304.
[6] Bobek T, Fackso S, Kurz H. Phys Rev B 2003;68:085324.
[7] Hofer C, Abermann S, Teichert C, Bobek T, Kurz H, Lyutovich K, et al. Nucl Instrum Meth B 2004;216:178.
[8] Rusponi S, Boragno C, Valbusa U. Phys Rev Lett 1997;78:2795.
[9] Shulga V. Nucl Instrum Meth B 2001;174:423.
[10] Valbusa U, Boragno C, Buatier de Mongeot F. J Phys: Condens Matter 2002;14:8153.
[11] Chan WL, Pavenayotin N, Chason E. Phys Rev B 2004;69:245413.
[12] Mayer TM, Chason E, Howard AJ. J Appl Phys 1994;76:1633.
[13] Asaro R, Tiller WA. Metall Trans 1972;3:1789.
[14] Srolovitz DJ. Acta Metall 1989;37:621.
[15] Spencer BJ, Voorhees PW, Davis SH. Phys Rev Lett 1991;67:3696.
[16] Freund LB, Jonsdottir F. J Mech Phys Solids 1993;41:1245.
[17] Yang WH, Srolovitz DJ. Phys Rev Lett 1993;71:1593.
[18] Xiang Y, Weinan E. J Appl Phys 2002;91:9414.
[19] Caturla MJ, de la Rubia TD, Marques LA, Gilmer GH. Phys Rev B 1996;54:16683.
[20] Flinn PA, Gardner DS, Nix WD. IEEE Trans Electron Dev 1987;34:689.
[21] Miyata H, Yamada T, Ferry DK. Appl Phys Lett 1993;62:2661.
[22] Nayak DK, Woo JCS, Park JS, Wang KL, MacWilliams KP. Appl Phys Lett 1993;62:2853.
[23] Takagi S, Hoyt JL, Welser JJ, Gibbons JF. J Appl Phys 1996;80:1567.
[24] Currie M, Leitz CW, Langdo TA, Tarashi G, Fitzgerald EA, Antoniadis DA. J Vac Sci Technol B 2001;19:2268.
[25] Keyes RW. J Phys D: Appl Phys 2002;35:L7.
[26] Fischetti MV, Gamiz F, Hansch W. J Appl Phys 2002;92:320.
[27] Thompson SE, Armstrong M, Auth C, Alavi M, Buehler M, Chau R, et al. IEEE Trans Electron Dev 2004;51:1790.
[28] Brantley WA. J Appl Phys 1973;44:534.
[29] Bifano TG, Johnson HT, Bierden P, Mali R. J MEMS 2002;11:592.
[30] d'Heurle FM. Metall Trans 1970;1:725.
[31] d'Heurle FM, Harper JME. Thin Solid Films 1989;171:81.
[32] Windischmann H. J Appl Phys 1987;62:1800.
[33] Windischmann H. Crit Rev Solid State Mater Sci 1992;17:547.
[34] Volkert CA. J Appl Phys 1991;70:3521.
[35] van Dillen T, Brongersma ML, Snoeks E, Polman A. Nucl Instrum Meth B 1999;148:221.
[36] Lee DH, Fayeulle S, Walter KC, Nastasi M. Nucl Instrum Meth B 1999;148:216.
[37] Zhang S, Johnson HT, Wagner GJ, Liu WK, Hsia KJ. Acta Mater 2003;51:5211.
[38] Erlebacher J, Aziz MJ, Chason E, Sinclair MB, Floro JA. Phys Rev Lett 1999;82:2330.
[39] Chason E, Erlebacher J, Aziz MJ, Floro JA, Sinclair MB. Nucl Instrum Meth B 2001;178:55.
[40] Chason E, Picraux ST, Poate JM, Borland JO, Current MI, de la Rubia TD, et al. J Appl Phys 1997;81:6513.
[41] de la Rubia TD, Gilmer GH. Phys Rev Lett 1995;74:2507.
[42] Barone ME, Graves DB. Plasma Sources Sci Technol 1996;5:187.
[43] Kubota NA, Economou DJ, Plimpton SJ. J Appl Phys 1998;83:4055.
[44] Kubota NA, Ecnonomou DJ. IEEE Trans Plasma Sci 1999;27:1416.
[45] Haddeman EFC, Thijsse BJ. Nucl Instrum Meth B 2003;202:161.
[46] Koster M, Urbassek HM. Nucl Instrum Meth B 2001;180:299.
[47] Kitabatake M, Greene JE. Thin Solid Films 1996;272:271.
[48] Chiba S, Aoki T, Matsuo J. Nucl Instrum Meth B 2001;180:317.
[49] Maric D, Colombo L. Mater Res Soc Symp Proc 1994;321:423.
[50] Marqués LA, Caturla MJ, Huang H, de la Rubia TD. Mater Res Soc Symp Proc 1996;396:201.
[51] Stillinger F, Weber T. Phys Rev B 1985;31:5262.
[52] Molière VG. Z Naturforschg 1947;2a:133.
[53] Torrens IM. Interatomic potentials. New York (NY): Academic Press; 1972.
[54] Zhu J, Yang L, Mailhiot C, de la Rubia TD, Gilmer GH. Nucl Instrum Meth B 1995;102:29.
[55] Delcorte A, Garrison BJ. J Phys Chem B 2000;104:6785.
[56] Smith R, Harrison Jr DE, Harrison BJ. Phys Rev B 1989;40:93.
[57] Frenkel D, Smit B. Understanding molecular simulation from algorithms to applications. 2nd ed. New York (NY): Academic Press; 2002.
[58] Berendsen H, Postma J, van Gunsteren F, DiNola A, Haak J. J Chem Phys 1984;81:3684.
[59] Nord J, Nordlund K, Keinonen J. Phys Rev B 2002;65:165329.
[60] Partyka P, Zhong Y, Nordlund K, Averback RS, Robinson IM, Ehrhart P. Phys Rev B 2001;64:235207.
[61] Machovà A. Modell Simul Mater Sci Eng 2001;9:327.
[62] Nielsen OH, Martin RM. Phys Rev B 1985;32:3780.
[63] Chandra N, Namilae S, Shet C. Phys Rev B 2004;69:094101.
[64] Tsai DH. J Chem Phys 1979;70:1375.
[65] Basinski ZS, Duesberry MS, Taylor R. Can J Phys 1971;49:2160.
[66] Hardy RJ. J Chem Phys 1982;76:622.
[67] Lutsko JF. J Appl Phys 1988;64:1152.
[68] Cheung KS, Yip S. J Appl Phys 1991;70:5688.
[69] Zimmermann JA, Webb III EB, Hoyt JJ, Jones RE, Klein PA, Bammann DJ. Modell Simul Mater Sci Eng 2004;12:S319.
[70] Cormier J, Rickman JM, Delph TJ. J Appl Phys 2001;89:99.
[71] Moore MC, Kalyanasundaram N, Freund JB, Johnson HT. Nucl Instrum Meth B 2004;225:241.
[72] Hull R. Properties of crystalline silicon. London: INSPEC IEE 91; 1999.